Received: 7 May 2023 | Revised: 10 November 2023 | Accepted: 16 January 2024

DOI: 10.1002/mp.16967

RESEARCH ARTICLE

MEDICAL PHYSICS

Automated multiclass segmentation, quantification, and visualization of the diseased aorta on hybrid PET/CT–SEQUOIA

Gijs D. van Praagh[1] | **Pieter H. Nienhuis**[1] | **Melanie Reijrink**[2] | **Mirjam E. J. Davidse**[3] | **Lisa M. Duff**[4] | **Bruce S. Spottiswoode**[5] | **Douwe J. Mulder**[2] | **Niek H. J. Prakken**[1] | **Andy F. Scarsbrook**[6,7,8] | **Ann W. Morgan**[6,7,8] | **Charalampos Tsoumpas**[1,4] | **Jelmer M. Wolterink**[3] | **Kim B. Mouridsen**[1,9] | **Ronald J. H. Borra**[1,10] | **Bhanu Sinha**[11] | **Riemer H. J. A. Slart**[1,12]

[1]Medical Imaging Center, Department of Nuclear Medicine & Molecular Imaging, University of Groningen, University Medical Center Groningen, Groningen, the Netherlands

[2]Department of Internal Medicine, division of Vascular Medicine, University of Groningen, University Medical Center Groningen, Groningen, the Netherlands

[3]Department of Applied Mathematics and Technical Medicine Center, University of Twente, Enschede, the Netherlands

[4]Faculty of Engineering and Physical Sciences, University of Leeds, Leeds, UK

[5]Siemens Medical Solutions USA, Inc., Knoxville, Tennessee, USA

[6]University of Leeds, School of Medicine, Leeds, UK

[7]NIHR Leeds Biomedical Research Centre, Leeds Teaching Hospitals NHS Trust, Leeds, UK

[8]NIHR Leeds Medtech and In vitro Diagnostics Co-operative, Leeds Teaching Hospitals NHS Trust, Leeds, UK

[9]Center of Functionally Integrative Neuroscience, Aarhus University, Aarhus, Denmark

[10]Department of Diagnostic Radiology, Turku University Hospital, Turku, Finland

[11]Department of Medical Microbiology and Infection Prevention, University of Groningen, University Medical Center Groningen, Groningen, the Netherlands

[12]Department of Biomedical Photonic Imaging, University of Twente, Enschede, the Netherlands

Correspondence
Gijs D van Praagh, Medical Imaging Center, Department of Nuclear Medicine and Molecular Imaging, University Medical Center Groningen, Hanzeplein 1, 9713 GZ, Groningen, the Netherlands.
Email: g.d.van.praagh@umcg.nl

Abstract

Background: Cardiovascular disease is the most common cause of death worldwide, including infection and inflammation related conditions. Multiple studies have demonstrated potential advantages of hybrid positron emission tomography combined with computed tomography (PET/CT) as an adjunct to current clinical inflammatory and infectious biochemical markers. To quantitatively analyze vascular diseases at PET/CT, robust segmentation of the aorta is necessary. However, manual segmentation is extremely time-consuming and labor-intensive.

Abbreviations: 2-[^{18}F]FDG, 2-deoxy-2-[^{18}F]fluoro-D-glucose; BA, Bland–Altman; DSC, dice similarity coefficient; EANM, European Association of Nuclear Medicine; HD, Hausdorff distance; HU, Hounsfield unit; ICC, intraclass correlation coefficient; IQR, interquartile range; LDCT, low-dose computed tomography; Na[^{18}F]F, sodium [^{18}F]fluoride; PET, positron emission tomography; SD, standard deviation; SEQUOIA, SEgmentation, QUantification, and visualizatiOn of the dIseased Aorta; SUV, standardized uptake value; TBR, target-to-background ratio.

Purpose: To investigate the feasibility and accuracy of an automated tool to segment and quantify multiple parts of the diseased aorta on unenhanced low-dose computed tomography (LDCT) as an anatomical reference for PET-assessed vascular disease.

Methods: A software pipeline was developed including automated segmentation using a 3D U-Net, calcium scoring, PET uptake quantification, background measurement, radiomics feature extraction, and 2D surface visualization of vessel wall calcium and tracer uptake distribution. To train the 3D U-Net, 352 non-contrast LDCTs from (2-[^{18}F]FDG and Na[^{18}F]F) PET/CTs performed in patients with various vascular pathologies with manual segmentation of the ascending aorta, aortic arch, descending aorta, and abdominal aorta were used. The last 22 consecutive scans were used as a hold-out internal test set. The remaining dataset was randomly split into training ($n = 264$; 80%) and validation ($n = 66$; 20%) sets. Further evaluation was performed on an external test set of 49 PET/CTs. The dice similarity coefficient (DSC) and Hausdorff distance (HD) were used to assess segmentation performance. Automatically obtained calcium scores and uptake values were compared with manual scoring obtained using clinical softwares (*syngo*.via and Affinity Viewer) in six patient images. intraclass correlation coefficients (ICC) were calculated to validate calcium and uptake values.

Results: Fully automated segmentation of the aorta using a 3D U-Net was feasible in LDCT obtained from PET/CT scans. The external test set yielded a DSC of 0.867 ± 0.030 and HD of 1.0 [0.6–1.4] mm, similar to an open-source model with a DSC of 0.864 ± 0.023 and HD of 1.4 [1.0–1.8] mm. Quantification of calcium and uptake values were in excellent agreement with clinical software (ICC: 1.00 [1.00–1.00] and 0.99 [0.93–1.00] for calcium and uptake values, respectively).

Conclusions: We present an automated pipeline to segment the ascending aorta, aortic arch, descending aorta, and abdominal aorta on LDCT from PET/CT and to accurately provide uptake values, calcium scores, background measurement, radiomics features, and a 2D visualization. We call this algorithm SEQUOIA (SEgmentation, QUantification, and visualizatiOn of the dIseased Aorta) and is available at https://github.com/UMCG-CVI/SEQUOIA. This model could augment the utility of aortic evaluation at PET/CT studies tremendously, irrespective of the tracer, and potentially provide fast and reliable quantification of cardiovascular diseases in clinical practice, both for primary diagnosis and disease monitoring.

KEYWORDS
aorta, artificial neural network, calcium score, cardiovascular disease, computed tomography, positron emission tomography, radiomics

1 | INTRODUCTION

Cardiovascular disease is the most common cause of death worldwide. In addition to atherosclerosis these include infection and inflammation-related diseases, for example, vascular graft infections and vasculitis.[1] Non-invasive imaging techniques play a central role in the identification, stratification, and follow-up of infectious and inflammatory vascular disease. Multimodality imaging, such as positron emission tomography (PET) and computed tomography (CT) of these diseases, allows physicians to observe molecular information PET in an anatomical context CT. PET imaging allows for the imaging of functional alterations, which frequently arise before the structural modifications that can be detected via CT imaging.[2]

Multiple studies have demonstrated potential advantages of hybrid PET/CT imaging in addition to conventional clinical inflammatory and infectious biomarkers. 2-Deoxy-2-[^{18}F]fluoro-D-glucose (2-[^{18}F]FDG) PET/CT is recommended for diagnosis of large vessel vasculitis and polymyalgia rheumatica and has higher diagnostic accuracy than conventional CT alone.[3,4] Furthermore, 2-[^{18}F]FDG-PET/CT has a valuable role in the non-invasive evaluation of suspected vascular graft infections.[5] Besides 2-[^{18}F]FDG, other potential vascular

tracers are increasingly being studied. For example, some studies have shown that increased uptake of sodium[^{18}F]fluoride (Na[^{18}F]F) is associated with higher cardiovascular risk.[6,7] Na[^{18}F]F binds to hydroxyapatite and is visible in active atherosclerosis progression, thus, PET/CT could prove useful for early diagnosis or even prediction of these diseases.[8,9]

Currently, vascular diseases are diagnosed mostly using visual assessment in clinic. The clinical utility of measurements such as standardized uptake values (SUV) or target-to-background ratios (TBR), is less established.[3,5] Some studies have demonstrated the potential for use of quantitative measurements. For example, cutoff values of SUV_{max} and TBR values had a high AUC of 0.83–0.94 for differentiating giant cell arteritis from control patients.[10–12] However, these are mostly small single center, retrospective studies and cut-off values differ between studies. To analyze aortic diseases more accurately at PET/CT, it is important to localize and quantitatively assess the aorta, for example, calcium in the aortic wall. Thus, aortic segmentation is needed. However, manual segmentation is time-consuming, labor-intensive, and prone to variability. This hinders large prospective studies utilizing quantitative measurements, causing a lack of standardization of these indices. As a result, translation of these indices into clinical practice is currently impossible. Therefore, automated segmentation and quantification is necessary.

(Semi-)automated organ segmentation reached clinical maturity, but most of the vascular software tools currently focus on diagnostic (contrast-enhanced) CT or magnetic resonance angiography.[2] This is due to the high image quality of these techniques and typical use of intravascular contrast agents, contrary to low-dose CT (LDCT) as often utilized in PET/CT. Recently, various groups have published segmentation models for (PET/)CT including the aorta.[13–16] However, these models only include the aorta as one full segment or only include the thoracic aorta, while many cardiovascular diseases manifest differently in different parts of the aorta.[17–19] Evidence on the exact metabolic activity in different segments of aortic diseases, such as large vessel vasculitis (giant cell arteritis, Takayasu arteritis) and atherosclerosis/(micro)calcifications, is limited or unevaluated.

Therefore, the aim of this study was to investigate the feasibility and accuracy of an automated tool to segment and quantify multiple parts of the diseased aorta on unenhanced LDCT as an anatomical reference for PET-assessed vascular disease.

2 | MATERIALS AND METHODS

2.1 | Study population and image acquisition

Our dataset included 352 retrospectively selected whole-body PET/CTs from four different cohorts: 38 2-[^{18}F]FDG-PET/CT scans of patients with diabetes mellitus from the RELEASE study[19]; 62 2-[^{18}F]FDG-PET/CT scans of patients with confirmed giant cell arteritis from the GPS cohort[20]; 235 clinical Na[^{18}F]F PET/CT scans; and 17 clinical 2-[^{18}F]FDG-PET/CT scans from patients with abdominal aortic aneurysms.[21] Due to its retrospective design, the medical research involving human subjects acts (WMO) obligation was waived by the local ethics committee (registration no. METC 2021/173). Therefore, objection registry was checked for all patients, but informed consent was not obtained. Data was stored and processed pseudonymized.

Imaging was performed on the following scanners: Biograph mCT40, Biograph mCT64, Biograph Vision, or Biograph Vision Quadra (Siemens Healthineers, Knoxville, TN, USA). See Table 1 for the patient characteristics and PET/CT scan parameters. 2-[^{18}F]FDG and Na[^{18}F]F PET/CT scans were performed following European Association of Nuclear Medicine (EANM) procedure guidelines.[22,23] After at least 6 h of fasting, 2 or 3 MBq/kg (dependent on scanner type) of tracer was intravenously administered to each patient. Sixty minutes after administration, an LDCT and subsequent PET scan from skull to knee, 1, 2, or 3 min per bed position (dependent on tracer and scanner type) or 10 min for the Biograph Vision Quadra, were performed.

2.2 | Manual segmentation

The aorta was manually segmented on the LDCT into four different regions (ascending aorta, aortic arch, descending aorta, and abdominal aorta) by four trained observers. Each dataset (as described above) was processed by one and the same MD(/PhD) student. The ascending aorta was delineated from the slice just above the aortic valve up to the first aortic branch, the aortic arch from the next slice up to and including the slice past the last aortic branch, the descending aorta from the next slice up to and including the diaphragm, and the abdominal aorta from the next slice up to the iliac bifurcation. All manual segmentations were performed using Affinity Viewer (version 2.0.3; Hermes Medical Solutions, Stockholm, Sweden) and were used as “ground truth”.

TABLE 1 Patient characteristics, PET/CT acquisition and reconstruction methods.

Characteristics	*N* (%) or mean ± SD or median (IQR)
No. of patients	352 (100)
Age (years) [range]	64.8 ± 15.1 [10–95]
Sex (males)	202 (57)
BMI (kg/m^2) [range]	26.8 ± 5.1 [15.1–46.6][a]
Cardiovascular disease	
Giant cell arteritis	64 (18)
Type 2 diabetes mellitus	62 (18)
Aneurysm/with stent	18 (5)/5 (1)
Situs Inversus	1 (0)
Oncology patients without cardiovascular disease	222 (63)
Radioactive tracers	
2-[^{18}F]FDG	117 (33)
Na[^{18}F]F	235 (67)
Scanners	
Biograph mCT40	97 (28)
Biograph mCT64	156 (44)
Biograph vision	95 (27)
Biograph vision quadra	4 (1)
Tube voltage (kV)	80 (N = 3), 100(N = 87), 120(N = 221), 140(N = 41)
Tube current time product (mAs)	14.5 (8.5–23.1)
Volumetric CT dose index (mGy)	0.9 (0.6–1.5)
Slice thickness (mm)	3
Matrix size (pixel × pixel)	512 × 512

Abbreviations: BMI, body mass index; IQR, interquartile range; SD, standard deviation.
[a]Of 24 patients, length and/or weight was unknown.

2.3 | Deep learning segmentation architecture and training

A four-layer 3D U-Net architecture was used to process one input channel and five output classes (one for every anatomical region and one for the background; see Figure 1).[24] To represent a clinical dataset the last consecutive 22 scans were used as a hold-out internal test set. The remaining dataset was randomly split into a training set (80%; n = 264), and a validation set (20%; n = 66). To optimize training, images were resampled to a voxel spacing of 0.97 × 0.97 × 1.5 mm^3, then cropped toward the center in *x-y* plane to 256 × 256 pixels, and inferior slices were cropped if the CT volume was larger than 700 slices. During training, all CT images were normalized based on window width/level settings of 600/100 Hounsfield units (HU), to improve contrast in the aorta. Data augmentation was used by random cropping to 160 × 160 × 64 voxels (156 × 156 × 94 mm^3; with a bias toward the center of the images), random rotation (between −5 and +5 degrees in transversal plane), and random Gaussian noise addition (with a mean of zero and a standard deviation [SD] between 0 and 6). The following training parameters were used: batch-size of 10, Adam optimizer with a learning rate of 0.001, and the dice similarity coefficient (DSC) loss. The model was trained for 200 epochs with an *early stopping* algorithm (and a 20-epoch patience). Before every epoch, the training dataset was randomly shuffled.

Predictions were performed using a sliding window with overlap, so that there were multiple predictions for each voxel, which were subsequently averaged. Small unconnected volumes (<10 mL) were removed from the prediction. The amount of overlap of the sliding window, that is, the number of predictions per voxel, and thereby the speed and accuracy of the model, can be adjusted by choosing a "fast" or "accurate" option. Unless differently specified, results of this article correspond to the "accurate" option. The "fast" option could make it feasible to process extremely large datasets.

All software code was written in Python (version 3.9, Python software foundation) using the open-source TensorFlow library with Keras API. The U-Net was trained on a 16 GB NVIDIA Tesla P100 GPU from a Microsoft Azure virtual machine (Microsoft, Redmont, WA, USA).

2.4 | External test

To test the performance of the algorithm on previously unseen data from a different center with different scanners, an external test set including 49 2-[^{18}F]FDG-PET/CTs from Leeds Teaching Hospitals National Health Service Trust performed in patients with suspected large vessel vasculitis was used; this cohort was reported upon previously.[25] Scans were acquired on three different scanners: Discovery 710, Discovery 690 (GE Healthcare, Chicago, IL, USA), or Gemini TF64 (Philips Healthcare, Best, the Netherlands). Prediction and analyses were performed in Leeds, so no data transfer agreement between the institutions was needed. In this previously published test set only the full aorta was segmented, so all classes were added together as a single label, and we were not able to perform a per segment analysis. Also, to compare the performance with a recently published open-source model (TotalSegmentator[15]), predictions of this model on this external test set were also compared with the manual segmentations (performed in Leeds too).

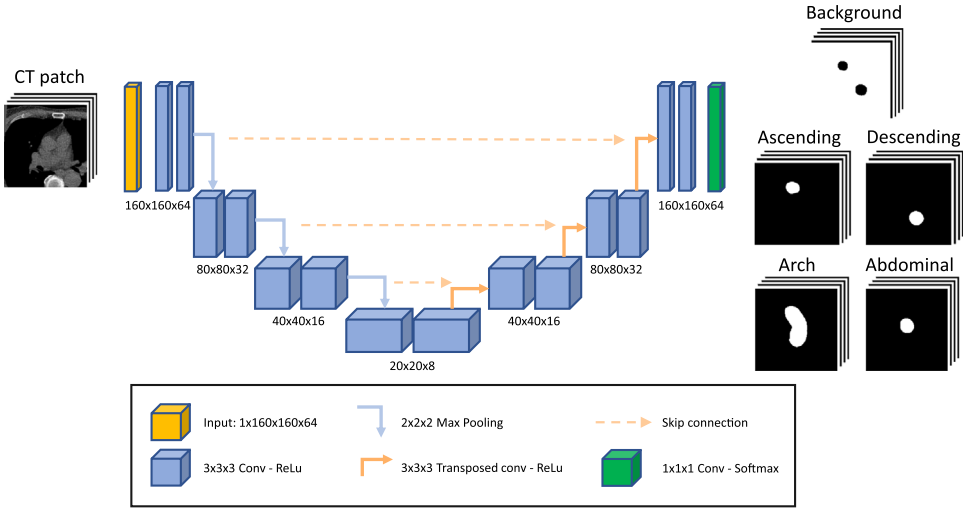

FIGURE 1 The used four-layer 3D U-Net architecture with convolutional steps, max pooling, transposed convolution, and corresponding skip connections. A softmax last layer was used. On the left an example of a 3D LDCT patch as input of the U-Net, and on the right an example of the corresponding five classes given as output.

2.5 | Automated prediction versus manual segmentations

The primary performance on both the internal and the external test set was assessed with the DSC and the average Hausdorff distance (HD). In addition, volumes of the predicted and manual segmentations were calculated. To assess clinical applicability, the segmentations were overlaid onto the CT to quantify calcium volume and calcium mass scores, and onto the co-registered PET images to measure SUV_{mean}, SUV_{max}, and SUV_{peak}. As Agatston scores can be heavily influenced by small differences in segmentations, these scores were not included for the segmentation comparison.

For the development and evaluation of the model, the recommendation of the Society of Nuclear Medicine and Molecular Imaging were followed as much as practically feasible and checks all boxes of the checklist for artificial intelligence in medical physics.[26–28]

2.6 | Calcium and SUV measurements

An earlier in-house developed and validated algorithm for a calcium phantom was adjusted to calculate Agatston scores, calcium volume scores, and calcium mass scores within the segmentations.[29] In that study, the calculation methods of four different manufacturers were extensively validated and included the international standard described by McCollough et al.[30] The algorithm was validated using clinical scans; 30 calcifications from six patients were manually scored on *syngo*.via (Siemens Healthineers, Knoxville, TN, USA) and compared to the automatically obtained scores. A mass calibration factor of 0.79 was used in both the algorithm and *syngo*.via. Calcifications which were partly outside the aorta, and thus not completely segmented, were excluded from analysis, for example, due to their progression in aortic branches or their connection with vertebrae.

The algorithm also included the measurements of SUV_{mean}, SUV_{max}, and SUV_{peak} in PET images. The SUV_{peak} measurements were determined in a sphere of 12 mm in diameter as described by Frings et al.[31] In the same patient images, the automatically obtained SUV measurements were compared with values obtained from the manual segmentations performed using Affinity Viewer. As Affinity Viewer only limits the center voxel of the SUV_{peak} sphere to the boundaries of the segmentations,[32] this was used for the validation. However, for further analyses, the entire sphere was limited to the boundaries of the segmentations to exclude high uptake from non-related surrounding tissue.

2.7 | Additional quantification functionality

The following additional functionality was added to the algorithm to assist future aortic PET/CT research:

1. Calcification measurements: the algorithm provides Agatston, volume, and mass scores for the entire aorta, per segment, and if wanted per calcification. There is also an option to calculate SUV_{mean}, SUV_{max}, and TBR values per calcification.
2. Radiomics features: the algorithm provides the possibility to automatically extract radiomics features per segment using PyRadiomics[33] which are stored in a

comma separated values file. Settings can easily be adjusted to need.

3. Background measurements: in the center of the ascending aorta a cylindrical volume of interest of around 1 mL is automatically extracted. Size, segment, and location of the volume can easily be adjusted.
4. 2D visualization: a visualization method was developed to show the calcium and PET tracer hotspot distribution. Within the full aorta segmentation simple thresholding was used to get images of aortic calcifications on CT and PET tracer uptake hotspots. Any thresholds can be chosen by the user. For CT: the standard 130 HU threshold according to the Agatston method,[34] a 147 HU threshold when 100 kVp is used as described by Nakazato et al.,[35] a patient specific threshold of the mean HU in the ascending aorta plus three times the SD of the background HU as described by Raggi et al.,[36] or any other HU value. For PET: any SUV value, or the background adapted 50% highest peak threshold of Frings et al..[37] A surface mesh of the full aorta was obtained using marching cubes. A map of calcium HU and SUV uptake on the aorta surface was obtained by outward projection of HU and uptake values from the centerline.

The algorithm was named SEQUOIA (SEgmentation, QUantification, and visualizatiOn of the dIseased Aorta; and refers to the vascular tree).

2.8 | Statistical analysis

Normally distributed data was presented as mean ± SD and non-parametric data as median (interquartile range [IQR]). All above-mentioned values from manual and automatically obtained values were statistically compared using Bland–Altman (BA) analysis, and the intraclass correlation coefficients (ICC) with absolute agreement. The BA analysis was performed with MATLAB (version R2018a, MathWorks, Natick, MA, USA), and ICC calculated using Statistical Package for Social Sciences (version 28, SPSS Inc., Chicago, IL, USA).

3 | RESULTS

Figure 2 shows the pipeline of SEQUOIA. This result section will go into each part in the order of the presented pipeline: segmentation, quantification, background measurement, and 2D visualization. As radiomics is a publicly available feature, we will not go into detail of that.

The developed software was tested on an Intel Xeon CPU E5-1620 with 32 GB RAM with an NVIDIA GeForce RTX 3060 GPU. Automated segmentations performed well compared to manual segmentations. For the "fast" or "accurate" option, segmentations took 102 ± 19 s or 370 ± 53 s (mean ± SD), respectively. Also, calcium and SUV measurements compared well with clinical software and including saving, the segments and background measurements took on average 40 ± 10 s per scan. The calculation time of the 2D visualization is dependent on the size of the aorta, and takes only 22 ± 9 s. The software has been made publicly available via GitHub under the Apache 2.0 license (https://github.com/UMCG-CVI/SEQUOIA).

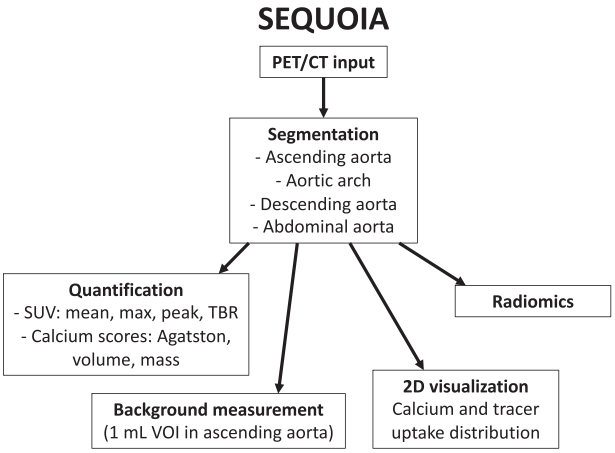

FIGURE 2 Pipeline of SEgmentation, QUantification, and visualizatiOn of the dIseased Aorta (SEQUOIA).

3.1 | Segmentation

3.1.1 | Internal test

Comparing the automated predictions of the U-Net with the manual segmentations of the internal test set, this resulted in a pooled DSC of 0.826 ± 0.075 (mean ± SD), and HD of 1.6 [1.2–2.5] mm (median [IQR]). Per segment this was 0.800 ± 0.090 and 2.1 [1.5–2.7] mm, 0.842 ± 0.054 and 1.3 [1.0–1.7] mm, 0.843 ± 0.067 and 1.6 [1.1–3.2] mm, and 0.820 ± 0.073 and 1.6 [1.2–2.6] mm for the ascending aorta, aortic arch, descending aorta, and abdominal aorta, respectively. When comparing all segments added together as one label, this resulted in a DSC of 0.885 ± 0.048, and HD of 1.2 [1.0, 1.5] mm. BA analysis showed a minor overall bias and small limits of agreement for label volume, SUV_{mean}, SUV_{max}, SUV_{peak}, calcium volume, and calcium mass scores (Table S1 and Figure S1). These figures and table also show negligible differences between the different segments.

3.1.2 | External test

Comparing manual segmentations from the test set with the automated predictions of the U-Net gave a similar DSC of 0.867 ± 0.030 (mean ± SD) and HD of 1.0

TABLE 2 Comparison external test set between manual segmentations and U-Net predictions ("accurate" and "fast" method) and manual segmentations and open-source model predictions.

		Manual versus U-Net ("accurate")	Manual versus U-Net ("fast")	Manual versus open-source model
DSC		0.867 ± 0.025	0.831 ± 0.038	0.864 ± 0.023
HD (mm)		1.0 [0.6 – 1.4]	1.2 [0.8 – 1.8]	1.4 [1.0 – 1.8]
Volume (mL)	BA	56.4 [9.1, 103.8]	88.9 [35.5, 142.4]	71.2 [31.4, 111.0]
	ICC	0.85 [−0.12 – 0.96]	0.70 [−0.08 – 0.92]	0.79 [−0.07 – 0.95]
SUV_{mean}	BA	0.0 [−0.1, 0.1]	0.0 [−0.1, 0.1]	0.0 [−0.1, 0.1]
	ICC	1.00 [1.00 – 1.00]	1.00 [0.99 – 1.00]	1.00 [1.00 – 1.00]
SUV_{max}	BA	1.6 [−3.6, 6.9]	1.8 [−3.5, 7.0]	1.5 [−2.9, 5.8]
	ICC	0.48 [0.06 – 0.71]	0.45 [0.02 – 0.69]	0.66 [0.27 – 0.83]
SUV_{peak}	BA	0.5 [−1.5, 2.6]	0.6 [−1.5, 2.6]	0.5 [−1.3, 2.2]
	ICC	0.63 [0.31 – 0.80]	0.61 [0.26 – 0.79]	0.75 [0.49 – 0.87]
Calcium volume (mL)	BA	0.8 [−3.4, 5.1]	1.4 [−4.2, 7.0]	1.7 [−3.2, 6.7]
	ICC	0.98 [0.96 – 0.99]	0.96 [0.90 – 0.98]	0.96 [0.86 – 0.98]
Calcium mass (g)	BA	0.2 [−1.2, 1.7]	0.4 [−1.5, 2.2]	0.4 [−0.8, 1.7]
	ICC	0.97 [0.94 – 0.98]	0.94 [0.87 – 0.97]	0.96 [0.89 – 0.99]

Note: Comparison was done using the Dice similarity coefficient, Bland-Altman bias and 95% limits of agreement, and intraclass correlation coefficient. Dice similarity coefficients are shown in mean ± SD. Bland-Altman and intraclass correlation coefficients are given in mean [95% confidence interval].
Abbreviatins: BA, Bland–Altman bias and 95% limits of agreement; DSC, dice similarity coefficient; HD, Hausdorff distance; ICC, intraclass correlation coefficient; SUV, standardized uptake value.

[0.6–1.4] mm (median [IQR]) (Table 2). For SUV_{mean}, SUV_{peak}, calcium volume, and calcium mass, variability (in terms of limits of agreement) was small. For SUV_{mean} no bias was noticed (0%). For volumes, SUV_{peak}, calcium volume, and calcium mass there was a consistent bias toward smaller predicted values of 14%−18% and a trend of increasing difference with larger size (Figure 3). For SUV_{max}, a larger bias toward smaller predicted values of 29% was observed, as well as relatively larger variability compared with other parameters. Figure 4 illustrates some predicted segmentations with proper outcome and some common mistakes. Figure S2 shows a screenshot of the image of one of the outliers from the SUV_{peak} plot, in which the manual segmentation included high uptake from the myocardium, which was not included in the prediction. Median ICC values ranged between 0.63 and 1.00.

For the "fast" option the U-Net predictions gave only a small reduction in accuracy in terms of DSC and HD (0.831 ± 0.038 and 1.2 [0.8–1.8] mm, respectively). BA biases and limits of agreement and ICC values were similar compared to the "accurate" results. Only the volume BA bias was larger and ICC value lower (Table 2).

Predictions of the open-source model resulted in similar DSC of 0.864 ± 0.023 and HD of 1.4 [1.0 – 1.8] mm. Also, BA plots showed similar results (Figure 3). Small variability was noticed, but even larger biases toward smaller predictions of 16%−29%. Again, no bias was seen for SUV_{mean} (0%). Median ICC values ranged between 0.75 and 1.00 (Table 2).

3.2 | Quantification

3.2.1 | Calcium and SUV measurements

Our software performed well when compared to the clinical software. Results for Agatston, calcium volume, and calcium mass scores showed small variability and only little bias toward smaller values of a few voxels (Figure 5). Five calcifications in the clinical software were detected and scored as two separate calcifications in our software (red crosses in Figure 5). This was because the clinical software connects the two calcifications with one single voxel in the *z*-plane (Figure S3). In our software, the calcification threshold was 1 mm^2 per slice to reduce the number of false positives due to noise, which resulted in at least two connected pixels. ICC (mean [95% CI]) values of Agatston, volume, and mass scores were 1.00 (1.00–1.00), 1.00 (1.00–1.00), and 1.00 (1.00–1.00), respectively.

Also, results for SUV measurements showed small variability and negligible bias of the SUV_{mean}, SUV_{max}, and SUV_{peak} of our software compared to clinical software (Figure 6). ICC values of SUV_{mean}, SUV_{max}, and SUV_{peak} were 0.96 (0.05–0.99), 0.99 (0.61–1.00), and 0.96 (0.84–0.99), respectively.

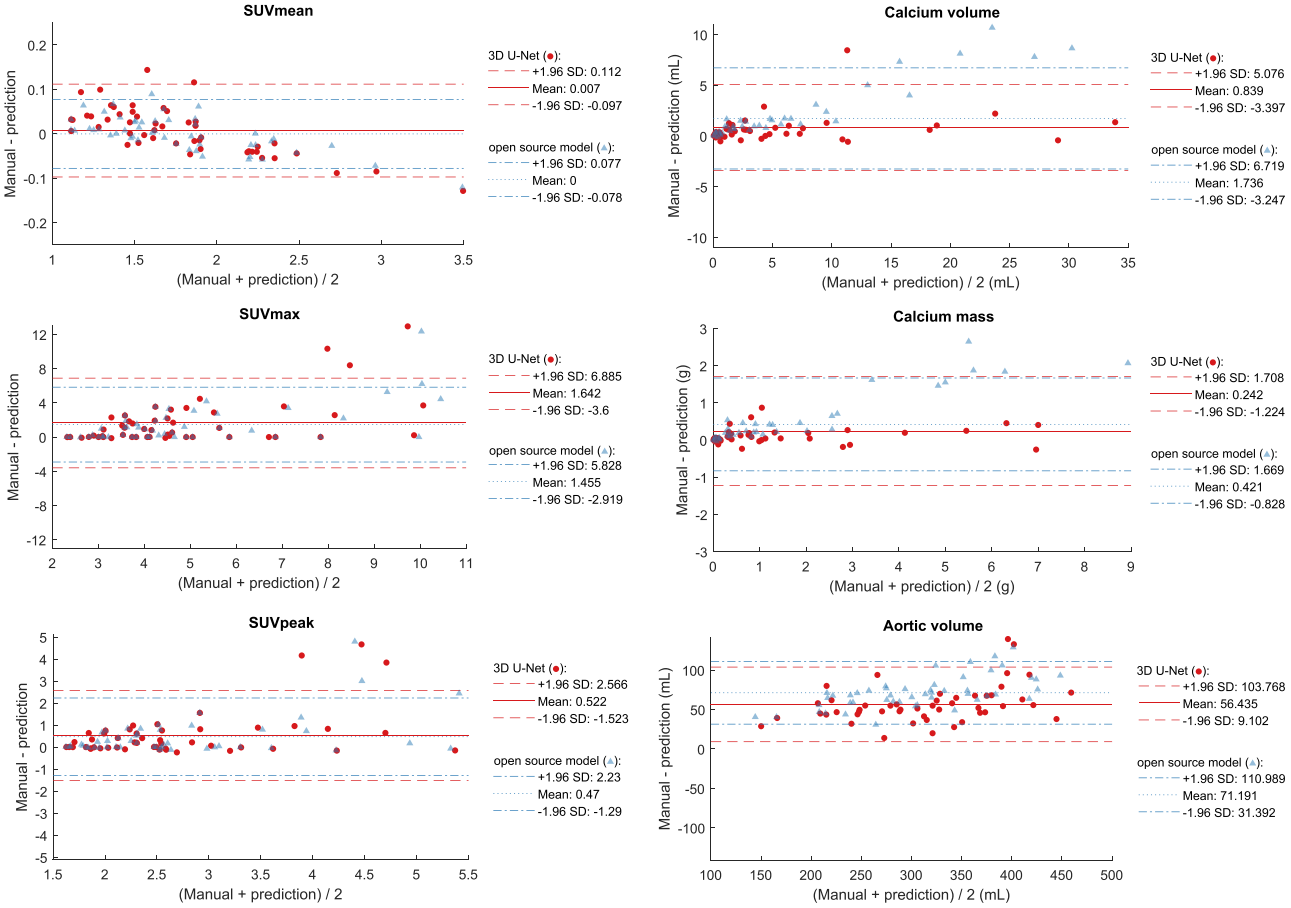

FIGURE 3 Bland–Altman plots of SUV_{mean}, SUV_{max}, SUV_{peak}, calcium volume, calcium mass, and full volume of the external test set. The dots (red) show the comparison between the manual segmentations and our 3D U-Net. The triangles (blue) show the comparison between the manual segmentations and the open-source model. Analysis could only be done for the full aortic volume.

3.3 | Background measurement and 2D visualization

3.3.1 | Additional quantification functionality

In Figure 7 and 8 an example of the background volume in the ascending aorta and 2D meshes of one of the external test set patients are shown. In the supplementary materials a video can be found (Video S1) and on the GitHub page of SEQUOIA two html files can be found to open the meshes in ParaView Glance. The meshes show the calcium distribution on CT and the distribution of 2-[^{18}F]FDG uptake hotspots in PET of one patient from the external test set.

4 | DISCUSSION

This study presents SEQUOIA, an open-source, automated, accurate, and fast model to segment the ascending aorta, aortic arch, descending aorta, and abdominal aorta on LDCT. Additionally, SEQUOIA automatically obtains calcium scores (Agatston, volume, and mass) and SUV measurements (mean, max, and peak) with excellent accuracy. The model performed well in an external test set from a different center acquired on three different scanners. Even though a substantially smaller training set was used, for the full aorta the model presented here performed equally well as a recently published open-source model.[15] However, in contrast to the open-source model, SEQUOIA provides multiple aortic segments, additional measurements, and was specially trained on low-dose data. Furthermore, to assist more research, background measurements, 2D visualizations of calcium CT and tracer PET distribution, and automatic radiomics feature extraction were added to the software. SEQUOIA has been made publicly available on GitHub.

Due to the time-consuming and labor-intensity characteristics of manual segmentation in large image data like PET/CT, the number of quantitative vascular studies is limited. The value of PET/CT in diagnosis or follow-up of vascular diseases is known. However, for

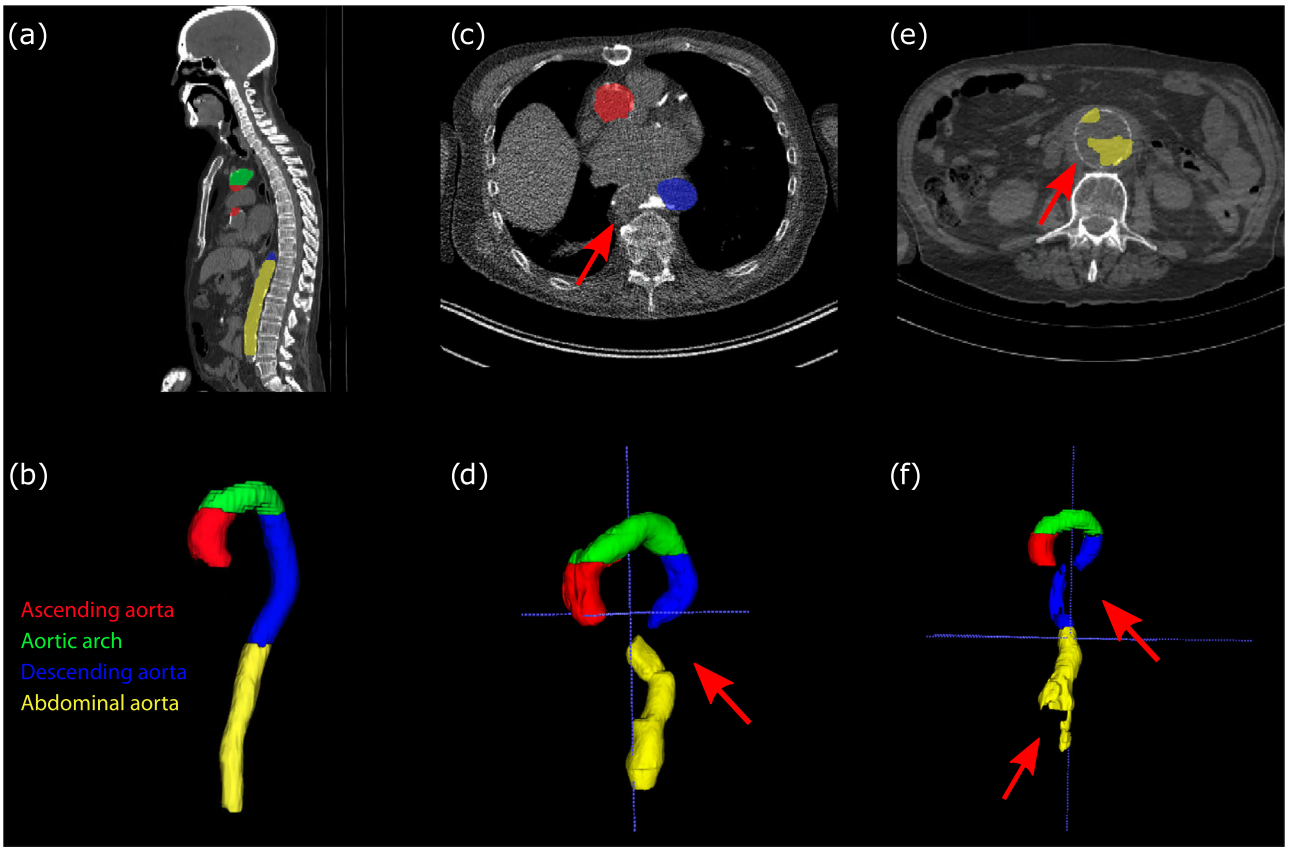

FIGURE 4 Examples of predictions from the U-Net: (a) and (b) an acceptable prediction; (c) and (d) erroneous gap between the descending and abdominal aorta due to unusual anatomy (the spiral morphology causes a sharp turn in the descending aorta close to the abdominal aorta unrecognized by the model as part of the aorta); (e) and (f) erroneous gaps in the descending aorta due to unusual anatomy and in the abdominal aorta due to a large aneurysm.

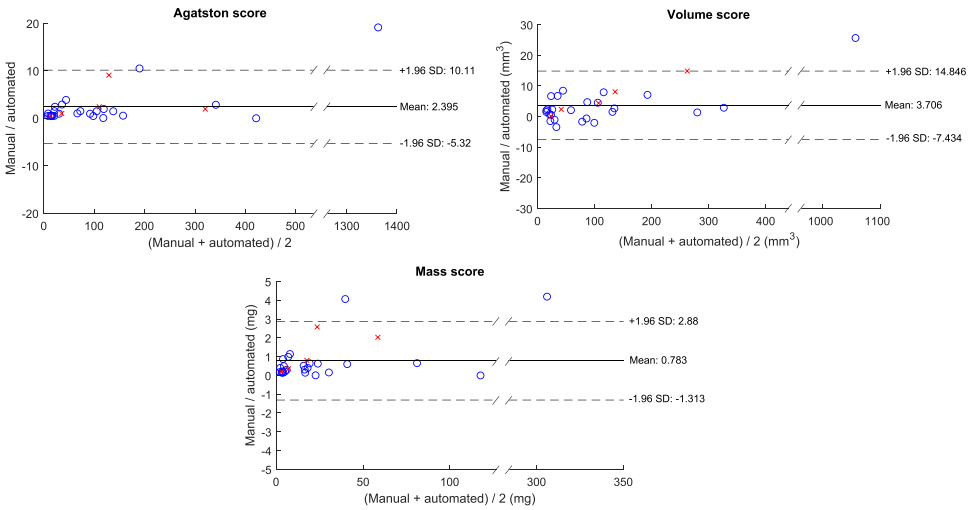

FIGURE 5 Bland–Altman plots of Agatston score, calcium volume score, and calcium mass scores in which the automated calcium scoring was compared to manual scoring from clinical software (syngo.via, Siemens Healthineers). The red crosses represent calcifications detected as one calcification by the clinical software, but as two separate calcifications by our automated software. This was due to a difference in threshold settings, resulting in one single voxel that connects (clinical software) or separates (our software) the two calcifications. The single outlier in the top right was caused by the same reason due to which some single voxels in this large calcification were missed.

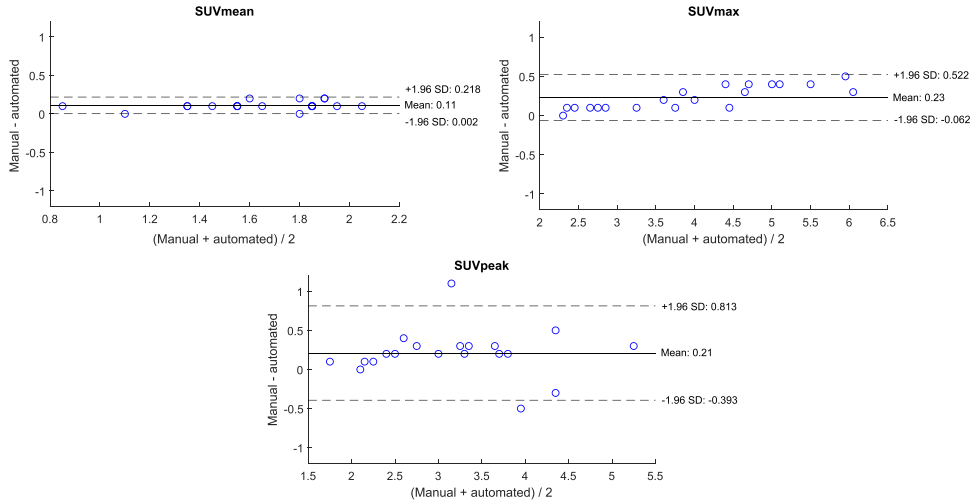

FIGURE 6 Bland–Altman plots of SUV_{mean}, SUV_{max}, and SUV_{peak} in which the automated calcium scoring was compared to manual scoring from clinical software (affinity viewer, Hermes medical solutions).

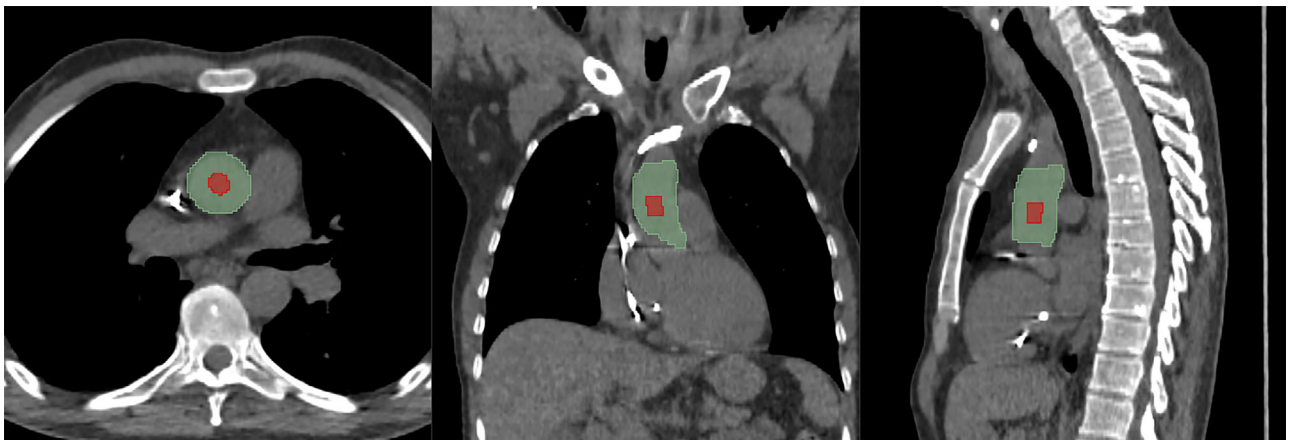

FIGURE 7 Axial, coronal, and sagittal planes through the CT image of a patient fused with the ascending aorta segmentation (green) and with background segmentation (red). Note that CT artifacts are due to a pacemaker lead in the vena cava.

many diseases there is no consensus yet on how to perform the quantification, and thus, how to use these measurements in diagnosis or risk assessment.[3,5,12] The European Association of Cardiovascular Imaging and the EANM recently stated that more research including the use of artificial intelligence is needed in this growing field.[38,39] The developed software program here could speed up aortic studies in nuclear medicine. This could help to better understand the metabolic mechanisms and the pathology of different vascular diseases in different parts of the aorta. For example, automatic segmentation and radiomics feature extraction might support studies to differentiate between inflammation and infection in possible vascular graft infections or infectious aneurysms.[40,41] This would also follow the latest recommendations of the EANM and the Society of Nuclear Medicine and Molecular Imaging to rely on automated segmentations, rather than manual delineation, for radiomics studies.[42]

Although the acquisition of LDCT from PET/CTs are not intended for accurate calcium analysis, this tool could help in a better understanding of the role of PET/CT in atherosclerosis. For example, in aortic studies the role of Na[^{18}F]F uptake in plaque vulnerability and calcium burden can be investigated. Together with the radiomics features it might help in differentiating between atherosclerosis and vasculitis as 2-[^{18}F]FDG uptake in both conditions can mimic each other.[43] Besides, as SEQUOIA is made in a modular pipeline, the calcium scoring algorithm can easily be used in higher dose CTs or different organ segmentations, for example, the coronaries.

Furthermore, the segmentation with background measurement in the ascending aorta is useful for reliably obtaining an image derived input function. This

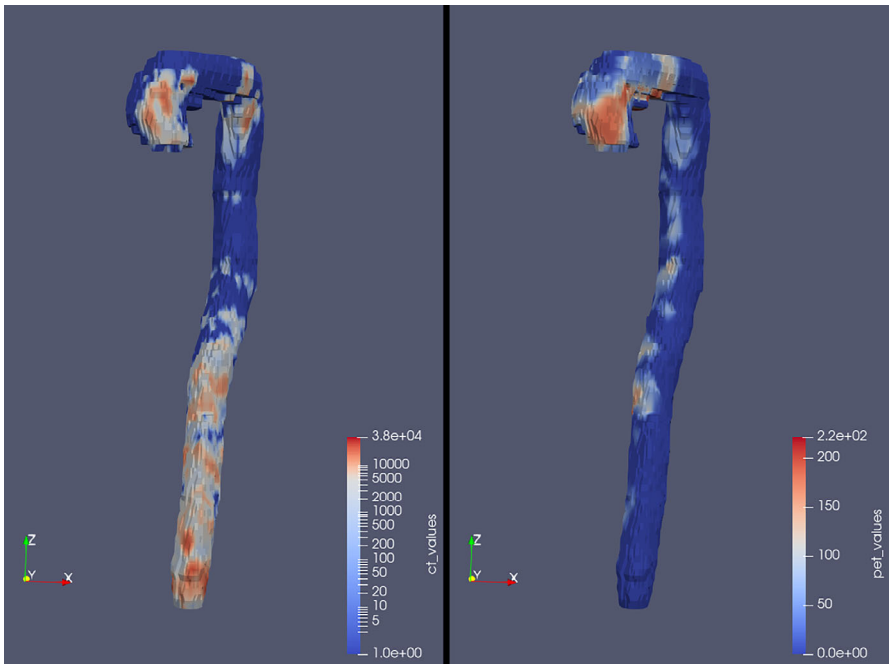

FIGURE 8 An example of two 2D surface meshes with the CT calcium distribution (left; in log scale) and the 2-[^{18}F]FDG uptake hotspot distribution (right). A video of these surface meshes can be found in the supplementary (Video S-1). HTML files can be found on the GitHub page (https://github.com/UMCG-CVI/SEQUOIA) to view these meshes in the interactive ParaView Glance tool.

is necessary to achieve automated kinetic analysis in PET/CT,[44] especially for long axial field-of-view PET scanners. This approach might prove useful in other diseases as well.[45] The 2D visualization may be used to illustrate differences to scans obtained in the context of longitudinal imaging, while those differences can be exactly measured in the segmentation volumes themselves.

Based on experience, segmenting one aorta took about 10–15 min. Assuming quantification, that is, calcium and SUV measurements, would also take about 10 min (in the best-case scenario) and an analyst is working effectively 8 h per day and 5 days a week, in theory all 330 aorta datasets in our dataset could be analyzed in about 20 days. Using our software with the "accurate" method, this could be done in about 1.5 days assuming the computer also works outside working hours. With the "fast" method this could even be done in less than half a day. Thus, the software speeds up result acquisition with at least 10–40 times, not taken into account the other work the person could do in the meantime.

Although other aortic segmentation models have been published,[13–16,25] to the best of our knowledge, this is the first software tool that automatically segments the ascending aorta, aortic arch, descending aorta, and abdominal aorta separately in PET/CTs in combination with an accurate calcium scoring algorithm and additional quantification features. Comparing our model with the manual segmentations from the test set, the model predictions resulted in on average 16% smaller total aortic volumes. This is similar to a previously published validation study of a CNN.[46] The open-source model even resulted in about 21% smaller volumes. Our results also demonstrated that this still gives comparable clinical values, like SUV_{mean}, SUV_{peak}, calcium volume, and calcium mass scores. The smaller volumes can probably be explained by three reasons. First, in the given spatial resolution, to ensure the entire aorta is included in the manual segmentation, some systematic bias might be introduced by segmenting the outer side of the wall. Second, compared with our model the manual segmentations from the test set started closer to the aortic valve in the ascending aorta, where our manual segmentations of the training set excluded that to avoid high myocardial uptake. We observed that some outliers were caused by including spill-over from the myocardium in the manual segmentation. Third, although we included various types of pathologies, the segmentation tool sometimes had some difficulties in recognizing the aorta due to large aneurysms or heavily calcified parts. These reasons also explain the divergence seen in Figure 3 for the SUV parameters. With larger volumes around the same pathology, SUV_{mean} will go down. As we observed some outliers in the manual segmentations including spill-over from surrounding tissue, differences in SUV_{max} and SUV_{peak} values will be larger causing bigger outliers. However, when the model will be regularly retrained, the robustness will increase. When using any model, including ours, one should always visually check the segmentation results before interpreting the clinical values, to avoid exclusion of regions of interest, or inclusion of adjacent organs.

This study has several limitations. First, the training dataset was relatively small and monocentric. However, the model performed well in an external set from different scanners and results were already comparable with an open-source model. Besides, regularly retraining the model will increase its accuracy and robustness. Second, segmentation accuracy was not assessed in an external test set for the four aortic segments separately due to a lack of appropriately labeled independent test data. Third, the calcium scoring algorithm could not be tested on CT scans from different manufacturers. However, results compared with commercially available software (*syngo*.via; Siemens Healthineers) were similar and the algorithm was previously extensively validated on different scanners with phantom scans.[29] Future studies should confirm that this tool works well on different CT scanners or acquisition settings before implementing the tool. Fourth, the calcium validation was only performed on a per calcification level, so no validation was performed on total scores per patient. This was done to exclude the influence of manual segmentation errors or anatomical deviations. Fifth, we did not include the vena cava as a class for segmentation and later target-to-background measurements. In future versions of the tool, the model can be extended to include the vena cava.

To conclude, we present SEQUOIA, an automated pipeline to segment the ascending aorta, aortic arch, descending aorta, and abdominal aorta on LDCT from PET/CT and to accurately provide PET-tracer uptake values, calcium scores, guided background measurements, radiomics features, and a 2D visualization. However, additional validation is needed for clinical applicability. This model may speed up aortic PET/CT studies tremendously, irrespective of the tracer, and potentially provide fast quantification of cardiovascular diseases and beyond in clinical practice in the future, both for primary diagnosis and disease monitoring.

ACKNOWLEDGMENTS

The authors have nothing to report.

CONFLICT OF INTEREST STATEMENT

G.D.v.P., B.S., R.H.J.A.S.: This study was in part supported by an unconditional grant from PUSH: a collaboration between Siemens Healthineers and the University Medical Center Groningen. The sponsor had no institutional role in the conceptualization, writing, or publication of the article. P.H.N., M.R., M.D., L.M.D., B.S.S., D.J.M., N.H.J.P., A.F.S., J.M.W., C.T., R.J.H.B., KBM: The authors have no conflicts to disclose. BSS: Full-time employee of Siemens Medical Solutions USA, Inc. AWM: Received salary support from the Medical Research Council (MRC) TARGET Partnership Grant (MR/N011775/1), NIHR Leeds Biomedical Research Centre (BRC), NIHR Leeds Medtech and in vitro Diagnostics Co-operative (MIC). This study was supported in part by the NIHR Leeds BRC, NIHR Leeds MIC and NIHR Senior Investigator Award. The views expressed are those of the authors and not necessarily those of the NIHR or the Department of Health and Social Care. Morgan also reports consultancy fees payable to her institution from Roche/Chugai, Sanofi/Regeneron, Glaxo Smith Kline, and AstraZeneca, outside the submitted work. Reports research and/or educational funding were received from Roche/Chugai and Kiniksa Pharmaceuticals, outside the submitted work.

DATA AVAILABILITY STATEMENT

The data that support the findings of this study are available from the corresponding author upon reasonable request. The data are not publicly available due to privacy or ethical restrictions. The software (SEQUOIA) has been made publicly available on GitHub (http://github.com/UMCG-CVI/SEQUOIA).

REFERENCES

1. Roth GA, Abate D, Abate KH, et al. Global, regional, and national age-sex-specific mortality for 282 causes of death in 195 countries and territories, 1980–2017: a systematic analysis for the Global Burden of Disease Study 2017. *The Lancet*. 2018;392(10159):1736-1788. doi:10.1016/S0140-6736(18)32203-7
2. Paravastu SS, Theng EH, Morris MA, et al. Artificial Intelligence in Vascular-PET: translational and Clinical Applications. *PET Clin*. 2022;17(1):95-113. doi:10.1016/j.cpet.2021.09.003
3. Slart RHJA, Glaudemans AWJM, Chareonthaitawee P, et al. FDG-PET/CT(A) imaging in large vessel vasculitis and polymyalgia rheumatica: joint procedural recommendation of the EANM, SNMMI, and the PET interest group (PIG), and endorsed by the ASNC. *Eur J Nucl Med Mol Imaging*. 2018;45(7):1250-1269. doi:10.1007/s00259-018-3973-8
4. Grayson PC, Alehashemi S, Bagheri AA, et al. 18 F-fluorodeoxyglucose-positron emission tomography as an imaging biomarker in a prospective, longitudinal cohort of patients with large vessel vasculitis. *Arthritis Rheumatol*. 2018;70(3):439-449. doi:10.1002/art.40379
5. Reinders Folmer EI, von Meijenfeldt GCI, te Riet ook genaamd Scholten RS, et al. A systematic review and meta-analysis of 18F-fluoro-d-deoxyglucose positron emission tomography interpretation methods in vascular graft and endograft infection. *J Vasc Surg*. 2020;72(6):2174-2185.e2. doi:10.1016/j.jvs.2020.05.065
6. Blomberg BA, de Jong PA, Thomassen A, et al. Thoracic aorta calcification but not inflammation is associated with increased cardiovascular disease risk: results of the CAMONA study. *Eur J Nucl Med Mol Imaging*. 2017;44(2):249-258. doi:10.1007/s00259-016-3552-9
7. Dweck MR, Chow MWL, Joshi NV, et al. Coronary Arterial 18F-Sodium Fluoride Uptake: a Novel Marker of Plaque Biology. *J Am Coll Cardiol*. 2012;59(17):1539-1548. doi:10.1016/j.jacc.2011.12.037
8. Czernin J, Satyamurthy N, Schiepers C. Molecular mechanisms of bone 18F-NaF deposition. *J Nucl Med*. 2010;51(12):1826-1829. doi:10.2967/jnumed.110.077933
9. McKenney-Drake ML, Moghbel MC, Paydary K, et al. 18F-NaF and 18F-FDG as molecular probes in the evaluation of atherosclerosis. *Eur J Nucl Med Mol Imaging*. 2018;45(12):2190-2200. doi:10.1007/s00259-018-4078-0

10. Prieto-González S, Depetris M, García-Martínez A, et al. Positron emission tomography assessment of large vessel inflammation in patients with newly diagnosed, biopsy-proven giant cell arteritis: a prospective, case–control study. *Ann Rheum Dis*. 2014;73(7):1388-1392. doi:10.1136/annrheumdis-2013-204572
11. Besson FL, De Boysson H, Parienti JJ, Bouvard G, Bienvenu B, Agostini D. Towards an optimal semiquantitative approach in giant cell arteritis: an 18F-FDG PET/CT case-control study. *Eur J Nucl Med Mol Imaging*. 2014;41(1):155-166. doi:10.1007/s00259-013-2545-1
12. Stellingwerff MD, Brouwer E, Lensen KJDF, et al. Different scoring methods of FDG PET/CT in giant cell arteritis need for standardization. *Med U S*. 2015;94(37):1-9. doi:10.1097/MD.0000000000001542
13. Trägårdh E, Borrelli P, Kaboteh R, et al. RECOMIA-a cloud-based platform for artificial intelligence research in nuclear medicine and radiology. *EJNMMI Phys*. 2020;7(1):51. doi:10.1186/s40658-020-00316-9
14. Sundar LKS, Yu J, Muzik O, et al. Fully automated, semantic segmentation of whole-body ^{18} F-FDG PET/CT images based on data-centric artificial intelligence. *J Nucl Med*. 2022;63(12):1941-1948. doi:10.2967/jnumed.122.264063
15. Wasserthal J, Breit HC, Meyer MT, et al. TotalSegmentator: robust segmentation of 104 anatomic structures in CT images. *Radiol Artif Intell*. 2023;5(5):e230024. doi:10.1148/ryai.230024
16. Noothout JMH, de VosBD, Wolterink JM, Išgum I. Automatic segmentation of thoracic aorta segments in low-dose chest CT. *Medical Imaging 2018: Image Processing*. SPIE 2018:446-451. doi:10.1117/12.2293114
17. Lie JT. Aortic and extracranial large vessel giant cell arteritis: a review of 72 cases with histopathologic documentation. *Semin Arthritis Rheum*. 1995;24(6):422-431. doi:10.1016/S0049-0172(95)80010-7
18. Stone JR, Bruneval P, Angelini A, et al. Consensus statement on surgical pathology of the aorta from the Society for Cardiovascular Pathology and the Association for European Cardiovascular Pathology: I. Inflammatory diseases. *Cardiovasc Pathol*. 2015;24(5):267-278. doi:10.1016/j.carpath.2015.05.001
19. de Boer SA, Hovinga-de Boer MC, Heerspink HJL, et al. Arterial stiffness is positively associated with 18F-fluorodeoxyglucose positron emission tomography–assessed subclinical vascular inflammation in people with early type 2 diabetes. *Diabetes Care*. 2016;39(8):1440-1447. doi:10.2337/dc16-0327
20. van Sleen Y, Therkildsen P, Nielsen BD, et al. Angiopoietin-2/-1 ratios and MMP-3 levels as an early warning sign for the presence of giant cell arteritis in patients with polymyalgia rheumatica. *Arthritis Res Ther*. 2022;24(1):1-10. doi:10.1186/s13075-022-02754-5
21. Liesker DJ, Mulder DJ, Wouthuyzen-Bakker M, et al. Patient-tailored approach for diagnostics and treatment of mycotic abdominal aortic aneurysm. *Ann Vasc Surg*. 2022;84:225-238. doi:10.1016/j.avsg.2022.01.006
22. Boellaard R, Delgado-Bolton R, Oyen WJG, et al. FDG PET/CT: EANM procedure guidelines for tumour imaging: version 2.0. *Eur J Nucl Med Mol Imaging*. 2015;42(2):328-354. doi:10.1007/s00259-014-2961-x
23. Beheshti M, Mottaghy FM, Paycha F, et al. (18)F-NaF PET/CT: EANM procedure guidelines for bone imaging. *Eur J Nucl Med Mol Imaging*. 2015;42(11):1767-1777. doi:10.1007/s00259-015-3138-y
24. Ronneberger O, Fischer P, Brox T. U-Net: convolutional networks for biomedical image segmentation. *IEEE Access*. 2015;9:16591-16603. doi:10.1109/ACCESS.2021.3053408
25. Duff LM, Scarsbrook AF, Ravikumar N, et al. An automated method for artifical intelligence assisted diagnosis of active aortitis using radiomic analysis of FDG PET-CT images. *Biomolecules*. 2023;13(2):343. doi:10.3390/biom13020343
26. Bradshaw TJ, Boellaard R, Dutta J, et al. Nuclear medicine and artificial intelligence: best practices for algorithm development. *J Nucl Med*. 2022;63(4):500-510. doi:10.2967/jnumed.121.262567
27. Jha AK, Bradshaw TJ, Buvat I, et al. Nuclear medicine and artificial intelligence: best practices for evaluation (the RELAINCE guidelines). *J Nucl Med*. 2022;63(9):1288-1299. doi:10.2967/jnumed.121.263239
28. El Naqa I, Boone JM, Benedict SH, et al. AI in medical physics: guidelines for publication. *Med Phys*. 2021;48(9):4711-4714. doi:10.1002/mp.15170
29. van Praagh GD, van der Werf NR, Wang J, et al. Fully automated quantification method (FQM) of coronary calcium in an anthropomorphic phantom. *Med Phys*. 2021;48(7):3730-3740. doi:10.1002/mp.14912
30. McCollough CH, Ulzheimer S, Halliburton SS, Shanneik K, White RD, Kalender WA. Coronary artery calcium: a multi-institutional, multimanufacturer international standard for quantification at cardiac CT. *Radiology*. 2007;243(2):527-538. doi:10.1148/radiol.2432050808
31. Frings V, van Velden FHP, Velasquez LM, et al. Repeatability of metabolically active tumor volume measurements with FDG PET/CT in advanced gastrointestinal malignancies: a multicenter study. *Radiology*. 2014;273(2):539-548. doi:10.1148/radiol.14132807
32. Hermes Medical Solutions. Affinity Handbook. Published online January 31, 2022.
33. van Griethuysen JJM, Fedorov A, Parmar C, et al. Computational radiomics system to decode the radiographic phenotype. *Cancer Res*. 2017;77(21):e104-e107. doi:10.1158/0008-5472.CAN-17-0339
34. Agatston AS, Janowitz WR, Hildner FJ, Zusmer NR, Viamonte M, Detrano R. Quantification of coronary artery calcium using ultrafast computed tomography. *J Am Coll Cardiol*. 1990;15(4):827-832. doi:10.1016/0735-1097(90)90282-T
35. Nakazato R, Dey D, Gutstein A, et al. Coronary artery calcium scoring using a reduced tube voltage and radiation dose protocol with dual-source computed tomography. *J Cardiovasc Comput Tomogr*. 2009;3(6):394-400. doi:10.1016/J.JCCT.2009.10.002
36. Raggi P, Callister TQ, Cooil B. Calcium scoring of the coronary artery by electron beam CT. *Am J Roentgenol*. 2002;178(2):497-502. doi:10.2214/ajr.178.2.1780497
37. Frings V, de Langen AJ, Smit EF, et al. Repeatability of metabolically active volume measurements with 18F-FDG and 18F-FLT PET in non-small cell lung cancer. *J Nucl Med*. 2010;51(12):1870-1877. doi:10.2967/jnumed.110.077255
38. Slart RHJA, Glaudemans AWJM, Gheysens O, et al. Procedural recommendations of cardiac PET/CT imaging: standardization in inflammatory-, infective-, infiltrative-, and innervation (4Is)-related cardiovascular diseases: a joint collaboration of the EACVI and the EANM. *Eur J Nucl Med Mol Imaging*. 2021;48(4):1016-1039. doi:10.1007/s00259-020-05066-5
39. Slart RHJA, Williams MC, Juarez-Orozco LE, et al. Position paper of the EACVI and EANM on artificial intelligence applications in multimodality cardiovascular imaging using SPECT/CT, PET/CT, and cardiac CT. *Eur J Nucl Med Mol Imaging*. 2021;48(5):1399-1413. doi:10.1007/s00259-021-05341-z
40. Saleem BR, Beukinga RJ, Boellaard R, et al. Textural features of 18F-fluorodeoxyglucose positron emission tomography scanning in diagnosing aortic prosthetic graft infection. *Eur J Nucl Med Mol Imaging*. 2017;44(5):886-894. doi:10.1007/s00259-016-3599-7
41. Husmann L, Huellner MW, Eberhard N, et al. PET/CT in therapy control of infective native aortic aneurysms. *Sci Rep*. 2021;11(1):5065. doi:10.1038/s41598-021-84658-z
42. Hatt M, Krizsan AK, Rahmim A, et al. Joint EANM/SNMMI guideline on radiomics in nuclear medicine. *Eur J Nucl Med Mol Imaging*. 2023;50(2):352-375. doi:10.1007/s00259-022-06001-6
43. Nienhuis PH, van Praagh GD, Glaudemans AWJM, Brouwer E, Slart RHJA. A review on the value of imaging in differentiating

between large vessel vasculitis and atherosclerosis. *J Pers Med*. 2021;11(3):236. doi:10.3390/jpm11030236
44. de Geus-Oei LF, Visser EP, Krabbe PFM, et al. Comparison of image-derived and arterial input functions for estimating the rate of glucose metabolism in therapy-monitoring 18F-FDG PET studies. *J Nucl Med*. 2006;47(6):945-949.
45. Slart R, Tsoumpas C, Glaudemans A, et al. Long axial field of view PET scanners: a road map to implementation and new possibilities. *Eur J Nucl Med Mol Imaging*. 2021;48(13):4236-4245. doi:10.1007/s00259-021-05461-6
46. Piri R, Edenbrandt L, Larsson M, et al. Aortic wall segmentation in 18F-sodium fluoride PET/CT scans: head-to-head comparison of artificial intelligence-based versus manual segmentation. *J Nucl Cardiol*. 2022;29(4):2001-2010. doi:10.1007/s12350-021-02649-z

SUPPORTING INFORMATION

Additional supporting information can be found online in the Supporting Information section at the end of this article.

How to cite this article: van Praagh GD, Nienhuis PH, Reijrink M, et al. Automated multiclass segmentation, quantification, and visualization of the diseased aorta on hybrid PET/CT–SEQUOIA. *Med Phys*. 2024;1-14. https://doi.org/10.1002/mp.16967